



1 **A foehn-induced haze front in Beijing: observations and implications**

2

3 Ju Li^{1*}, Zhaobin Sun¹, Donald H. Lenschow², Mingyu Zhou³, Youjun Dou¹, Zhigang Cheng¹,

4 Yaoting Wang¹, Qingchun Li¹

5

6 ¹ Institute of Urban Meteorology, Beijing, China

7 ² National Center for Atmospheric Research, Boulder, CO, USA

8 ³ National Marine Environment Forecast Center, Beijing, China

9 *Correspondence to: Ju Li (jli@ium.cn)

10 **Abstract.** Despite frequent foehns in the Beijing-Tianjin-Hebei (BTH) region, there are only a few
11 studies of their effects on air pollution in this region, or elsewhere. Here, we discuss a
12 foehn-induced haze front (HF) event using observational data to document its structure and
13 evolution. Using a dense network of comprehensive measurements in the BTH region, our
14 analyses indicate that the foehn played an important role in the formation of the HF with
15 significant impacts on air pollution. Northerly warm-dry foehn winds, with low particulate
16 concentration in the northern area, collided with a cold-wet polluted air mass to the south and
17 formed an HF in the urban area. The HF, which is associated with a surface wind convergence line
18 and distinct contrasts of temperatures, humidity and pollutant concentrations, resulted in an
19 explosive growth of particulate concentration. As the plains-mountain wind circulation was
20 overpowered by the foehn, a weak pressure gradient due to the different air densities between air
21 masses was the main factor forcing advances of the polluted air mass into the clean air mass,
22 resulting in severe air pollution over the main urban areas. Our results show that the foehn can
23 affect air pollution through two effects: direct wind transport of air pollutants, and altering the air
24 mass properties to inhibit boundary-layer growth and thus indirectly aggravating air pollution.
25 This study highlights the need to further investigate the foehn and its impacts on air pollution in
26 the BTH region.

27

28

29

30



31 1 Introduction

32 Air pollution issues in China have been widely discussed and studied in recent decades. The
33 region encompassing Beijing City, Tianjin City, and Hebei province, i.e. the Beijing-Tianjin-Hebei
34 (BTH) region, is one of most polluted areas in China and has a very high level of particular matter
35 of 2.5 μm diameter ($\text{PM}_{2.5}$) (Han et al., 2014; Gao et al., 2015; Jiang et al., 2015a; Wang et al.,
36 2015). Furthermore, severe haze events occur frequently in the BTH region, especially in autumn
37 and winter (Wang et al., 2013; Sun et al., 2014; Sun et al., 2016; Zhang et al., 2015; Li et al., 2016;
38 Li et al., 2017), and negatively affect human health (Guo et al., 2017). Stagnant weather
39 conditions and large anthropogenic emissions in this region are the main reasons for heavy haze
40 and pollution (Zhao et al., 2013; Liu et al., 2013; Wang et al., 2013; Zhang et al., 2014; Zhang et
41 al., 2015; Liu et al., 2017). Previous studies have shown feedbacks between aerosol and
42 meteorological variables (e.g., Steiner et al., 2013; Tie et al., 2017; Huang et al., 2018; Li et al.,
43 2018a; Wu et al., 2019). A high concentration of $\text{PM}_{2.5}$ can weaken turbulence (Ren et al., 2019)
44 and enhance stability in the planetary boundary layer (PBL) resulting in decreased PBL height and
45 consequently increased $\text{PM}_{2.5}$ concentrations (Su et al., 2018), i.e. a positive feedback between
46 aerosols and PBL height (Petäjä et al., 2016). Liu et al. (2018) found another positive feedback:
47 decreased PBL height can increase relative humidity (RH), and, in turn enhance secondary aerosol
48 (SA) formation and further enhance particulate concentration, weaken solar radiation, and further
49 decrease PBL height.

50 During severe haze events in the BTH region, $\text{PM}_{2.5}$ concentrations can increase as much as
51 $200 \mu\text{g}\cdot\text{m}^{-3}$ in several hours (Zhong et al., 2017). On the one hand, SA formation through aerosol
52 hygroscopic growth is one of main reasons causing this explosive growth of particular matter (Han
53 et al., 2015; Sun et al., 2014; Chen et al., 2019). Huang et al. (2014), for example, found that
54 severe haze pollution events were mostly the result of SA. On the other hand, vertical and
55 horizontal transport can also produce an explosive growth of particular matter. Observations have
56 shown that downward transport by large coherent eddies produced explosive growth of surface
57 $\text{PM}_{2.5}$ concentrations (Han et al., 2018; Li et al., 2018b). Complex topography, land-use and
58 land-cover, e.g. the Taihang and Yan Mountains, the Jing-Jin-Ji city cluster and Bohai Bay in BTH
59 region, can also induce local circulations that affect air pollutant concentrations (Liu et al., 2009;
60 Wang et al., 2017). The distribution of air pollutants in Beijing and Tianjin is readily modified by
61 mountain-valley breezes and sea-land breezes. Regional transport by local-scale and weather-scale
62 wind systems contribute significantly to the formation of severe haze events in the BTH region
63 (Zheng et al., 2015; Sun et al., 2016; Ma et al., 2017; Jiang et al., 2015b). Dang et al. (2019)
64 reported that regional transport was the most important process for the formation of severe winter
65 haze days in the BTH region with a relative contribution of 65.3%. Transport of aerosols to the
66 BTH region by multi-scale circulations was also reported by Miao et al. (2017). However, due to a
67 lack of dense vertical and horizontal spatial coverage of meteorological and aerosol observations,
68 aerosol transport mechanisms and their effect on the explosive growth of particular matter in the
69 BTH region are uncertain on both urban and smaller scales.

70 During a severe haze pollution event in 2015 in Beijing, a haze front (HF) phenomenon was
71 reported on an internet social network, and also was intensively observed e.g. by scanning lidars
72 and instrument networks during the 3-year field campaign of the Study of Urban Rainfall and
73 Fog/Haze (SURF; Liang et al., 2018). The haze front resulted in $\text{PM}_{2.5}$ concentration increases of
74 more than $200 \mu\text{g}\cdot\text{m}^{-3}$ in a half hour or less when it passed over. This visible haze front in Beijing



75 resembles the smog front noted by Ahrens (2003) but differs in that its formation mechanism is
76 foehn winds. The foehn is characterized by a decrease in cloudiness on the lee side of mountains
77 and warm, dry, strong and gusty winds (Brinkmann 1971; Richner and Hächler 2013). The foehn
78 warming mechanisms are summarized into four types (Elvidge and Renfrew 2016): isentropic
79 drawdown, latent heating and precipitation, mechanical mixing due to turbulence, and radiative
80 heating. Foehns occur downstream of most major mountain ridges in the world (Drechsel and
81 Mayr 2008; Nkemdirim and Leggat 1978; Norte 2015; Takane and Kusaka 2011; Zhao et al.,
82 1993). Beijing city is located on the plains adjacent to the southwest-northeast oriented Taihang
83 Mountains and the northwest-southeast oriented Yan Mountains to the west and north, respectively.
84 Due to this topography, Beijing is often affected by foehns especially in the plains areas adjacent
85 to the mountains (Li et al., 2016, Wang et al., 2012a, 2012b). The temperature can increase sharply
86 in a short time: for example, Luo et al. has reported an intense foehn warming event in which
87 surface air temperature increased by more than 10°C per hour in Beijing (Luo et al., 2020).
88 Despite the fact that the foehn has been investigated for a long time, there are few studies of the
89 influence of foehns on air pollution, especially in BTH region which has, for decades, been a
90 worldwide hotspot for studying air pollution (Gohm et al. 2009; Li et al. 2015; McGowan et al.
91 1996, 2002). Also, very few studies have reported foehn-related fronts. Vergeiner (2004) reported
92 a “minifront” or a convergence line between the up-valley flow and the down-valley foehn flow
93 that was maintained near the surface layer in the Wipp Valley, Austria. Li et al. (2015) found that a
94 ground-based foehn colliding with a thermally-driven valley breeze formed a “minifront” in
95 Urumqi, China, indicating that the foehn can play a critical role in the formation of severe air
96 pollution events in this area. Nonetheless, foehn-related haze fronts seem to have never been
97 investigated in the BTH region. Foehns usually come from western, northwestern and northern
98 mountain areas in the Heibei-Beijing region, which are usually less polluted than the plains area in
99 this region. Hence, foehns tend to increase visibility and decrease PM_{2.5} concentrations in plains
100 areas (Yang et al., 2018). In our case study, the foehn initially decreased PM_{2.5} concentrations in
101 the northern plains area of Beijing, and then interacted with a polluted air mass leading to severe
102 pollution in the urban area. This latter dramatic consequence has not been reported in previous
103 studies. The goal of our study is to investigate the structure and formation of this foehn-related
104 haze front on small scales in order to improve our understanding of the role of the foehn in air
105 pollution events in the BTH region. Intensive measurements from SURF as well as routine
106 measurements across the BTH region and historic data sets are described in Sect. 2. In Sect. 3, we
107 examine the characteristics and evolution of the haze front. In Sect. 4, we compare the formation
108 of a sea breeze front and a haze front, discuss the main reason for HF propagation and the role of
109 the foehn on air pollution. Sect. 5 is a summary.

110

111 2 Instrumentation, observations and data

112 Figure 1 and Table 1 shows the main observation sites mentioned here. The IAP site, which has
113 been operated by the Institute of Atmospheric Physics (IAP) since 1978, has a 325 m high
114 meteorological tower collocated with a ground-based Doppler lidar (Windcube 100S, Leosphere)
115 and a mini-micropulse aerosol lidar (mini-MPL, SigmaSpace). The Doppler lidar profiled the
116 mean wind using the Doppler beam swing (DBS) scan mode. The mini-MPL lidar profiled
117 aerosols and normalized relative backscatter (NRB). Wind direction and speed, air temperature,
118 and relative humidity were measured at 15 levels (8, 15, 32, 47, 65, 80, 100, 120, 140, 160, 180,



119 200, 240, 280, 320 m) on the tower. Three-dimensional sonic anemometers, downward- and
120 upward-pointing pyrogeometers and pyranometers (CNR1, Kipp & Zonen) and CO₂/H₂O
121 concentration sensors (LI-7500) were installed at 47 m, 140 m and 280 m. The instrumentation at
122 the IAP site is described in detail by Li et al. (2018b).

123 A mini-MPL lidar was installed at the top of the office building of the Institute of Urban
124 Meteorology (IUM), executing a plan-position indicator (PPI) scan mode at a 5° elevation angle
125 and every 10° of azimuth angle from 230° to 340° (Fig. 5d). An air quality station on the ground
126 ~ 40 m south of the IUM office building provided 5-minute mean PM_{2.5} concentrations. A weather
127 camera facing west was also installed in a room on the 9th floor of the office building taking
128 photos every 30 s. Due to the absence of a surface weather station at the IUM site, meteorological
129 data every 5 minutes from an automated weather station (AWS) at the Chedougou (CDG) site, ~ 1
130 km north of the IUM site, was jointly analyzed with data at IUM. An operational wind profiler
131 was installed at the Haidian (HD) National Weather station site. We also used radio soundings
132 launched twice daily at the Guanxiangtai (GXT) site. Hourly observations of PM_{2.5} from all the
133 air quality stations were obtained from the website of the Ministry of Ecology and Environmental
134 of the People's Republic of China (<http://106.37.208.233:20035>). We used hourly PM_{2.5} data at
135 Aotizhongxin (AOT) site, ~3 km northeast of the IAP site, and Yizhuang (YZ) site, ~4 km
136 northeast of the GXT site, to roughly represent PM_{2.5} concentrations at IAP and GXT, respectively.
137 At the Changping (CP) site, the AWS of the Beijing Meteorology Service (BMS) is very close to
138 the air quality station of Beijing Municipal Ecological Environment Bureau (BMEEB). During the
139 study period, the Himawari satellite provided cloud images over the Beijing area every 10 minutes.
140 The pictures of this infrequent haze front were initially released by internet social communities,
141 e.g. SINA Weibo (equivalent to Chinese Twitter). Based on time and location information, we
142 selected two photos shown in Figure 1. All the observation heights used in this study are from
143 ground level (AGL). Also, in order to investigate foehn occurrence frequency and its relationship
144 to PM_{2.5} concentrations in Beijing, 1 year AWS data at CP, AOT and GXT, and PM_{2.5} data at CP,
145 AOT and YZ from 1 March 2015 to 29 February 2016 are used.

147 3 The evolution and characteristics of the haze front

148 3.1 Regional background of air pollution and weather conditions

149 This HF occurred on 24 December 2015 concurrent with a severe air pollution episode. The mean
150 PM_{2.5} concentrations in Beijing varied between 300–400 μg m⁻³ in the morning on 23 December, a
151 severe Air Quality Index (AQI) pollution level (Fig. 2a). Thereafter, the PM_{2.5} concentration
152 decreased to ~100 μg m⁻³ at 08:00 LST on 24 December and increased steadily up to 500 μg m⁻³
153 by afternoon of the next day. A 500 mb trough passed Beijing at 08:00 LST on 24 December (Fig.
154 3a). Winds were predominantly westerly or northwesterly at ~ 500 m AGL (Figure 2a, 2b, 2d). On
155 the surface, a weak cold front was west of Beijing. On the right-side of the cold front, fog was
156 reported in Hebei and Shandong Provinces, and easterly flow was reported in Beijing by surface
157 meteorological stations. At 20:00 LST, there was a weak surface high centered north of Beijing.
158 The pressure gradient was weak with weak southwesterly surface flow in Beijing (Fig. 2c, Fig.
159 3f).

160 3.2 The evolution of the HF

161 The visible channel images from the Himawari satellite clearly showed the movement and
162 evolution of the HF as well as fog—dense white fog covered northeastern Tianjin and half of



163 Xianghe county of Hebei Province at 08:00 LST (Fig. 4a). Meanwhile, the Beijing area was clear
164 with low pollution. Southwest-northeast oriented clouds partly shadowed the fog in Tianjin and
165 Bohai Bay. Left of the fog front, the gray-white shading indicated hazy air with its front extending
166 just into the boundary of Beijing. The edge of the hazy air mass corresponding to the HF line
167 began to impact the GXT site (the blue dot, Fig. 4b, Fig. 11) at 10:00 LST followed by expanding
168 fog areas. The HF line moved slowly to the northwest while fog areas shrank quickly due to
169 increasing solar radiation. A west-east oriented high cloud street overlapped the hazy and foggy
170 areas (Fig 4d). After 16:00 LST, the fog disappeared and the HF line subsequently impacted the
171 FS, CBD and IUM sites (Fig. 1, Fig. 5), leaving a smaller unpolluted urban area on the
172 northwestern plains area in Beijing.

173 The Min-MPL at IUM scanned the HF passage using the PPI mode (Fig. 5c). The lidar initially
174 detected a hazy air mass to the southwest far away from the lidar site. As the HF approached, the
175 outline of the polluted air mass was clearly visible against the sky and buildings on the weather
176 camera photos (t1, Fig. 5e). When the HF arrived at the IUM site, the building view was blurred
177 by the hazy air mass (t2, Fig. 5e). Surface wind direction changed suddenly from NNW to WSW.
178 The $PM_{2.5}$ concentration jumped from ~ 10 to $269 \mu\text{g m}^{-3}$ in 10 minutes (Fig. 5b). The wind
179 direction suddenly changed to northerly at 16:30 LST resulting in an abrupt $PM_{2.5}$ concentration
180 decrease to $11 \mu\text{g m}^{-3}$ (Fig. 5b) and the visibility increased as evidenced by some visible buildings
181 (t3, Fig. 5e). In less than 10 minutes, the wind direction reverted again from N to NNW resulting
182 in a $PM_{2.5}$ concentration increase to $106 \mu\text{g m}^{-3}$ (Fig. 5b) and again blurred the building view at
183 16:39 LST (t4, Fig. 5e). The scans showed five pollution ‘waves’ successively touched down at
184 the site and consequently led to severe pollution at 19:30 LST at IUM (Fig. 5b, 5c). The IAP site,
185 8 km northeast of IUM, was affected by the hazy air mass at around 20:30 LST according to
186 vertically scanning lidar observations at this site (Fig. 5a).

187 Based on the dense AWSs and air quality monitoring station coverage, we were able to analyze
188 surface distribution patterns of air temperature and humidity as they were affected by air flows and
189 $PM_{2.5}$ concentrations in the plains areas. The HF line was identified by temperature and humidity
190 contrasts between the warm and cold air masses and the convergence line of the surface wind field
191 (Fig. 6-7, Fig. S1-S3), which was also consistent with the front edge of the hazy air mass seen in
192 the satellite images (Fig. 4). The warm, dry, and clean air mass with more northerly winds was
193 surrounded by the cold, wet, and polluted air mass with more southerly or southeasterly winds
194 (Fig. 6-7). The position of the HF line oscillated due to the collision between the two air masses.
195 The HF line slowly advanced northwesterly with the southern part moving at about 2.5 km h^{-1} (Fig.
196 6). The $PM_{2.5}$ contrast between the two air masses was more than $200 \mu\text{g m}^{-3}$. At 16:00 LST, the
197 west-east oriented HF line crossed the main urban area and reached the IUM site. Later that night,
198 the wet and hazy air mass overlay most of the plains except for a small area on the northwestern
199 plains adjacent to the mountains (e.g., the CP site). As the foehn began to decrease and retreat, and
200 radiative heating decreased in late afternoon, the warm-dry air mass became weaker and shrank,
201 leading to dissolution of the HF. After the northerly gusty winds decreased after sunset, the
202 polluted air mass moved quickly toward the relative warm-dry and clean areas, resulting in severe
203 pollution over most of the plains areas in Beijing.

204

205 3.3 Characteristics of the HF and foehn winds



206 We used the CP, CDG and GXT sites (locations in Fig. 1) to investigate characteristics before and
207 after the hazy air mass passed through. The northernmost site CP was mostly unaffected by the
208 hazy air mass during 24 December. The southernmost site GXT was affected by the hazy air mass
209 the earliest at 10:00 LST on 24 December. Afterward, the $PM_{2.5}$ concentration at GXT varied from
210 349 to 515 $\mu\text{g m}^{-3}$ until midnight (Fig. 8e). The $PM_{2.5}$ concentration at CP was the lowest among
211 three sites with a maximum of 148 $\mu\text{g m}^{-3}$ at 11:00 LST and a minimum of 26 $\mu\text{g m}^{-3}$ at 15:00 LST.
212 The three-hourly temperature tendency showed that air temperature at CP increased significantly
213 at 11:00 LST due to the foehn; in contrast, air temperatures decreased significantly at CDG and
214 GXT. Meanwhile, humidity decreased and wind speed increased at CP due to the foehn. The warm
215 and dry foehn wind was initially detected over the northwestern mountains and plains of
216 Changping County at around 11:00 LST, with a significant increase in temperature and the north
217 wind component, and decrease in humidity. Wind profiler observations at HD also showed
218 enhanced upper-air winds. From 10:00 to 13:00 LST, air temperature increased from 1.9°C to 6°C,
219 relative humidity decreased from 49% to 24%, and wind speed increased from 1 m/s to 4.6 m/s at
220 CP. The foehn affected CDG at about 12:00 LST and IAP at 13:00 LST before colliding with a
221 cold, wet, and hazy air mass. At 11:00 LST, an urban heat island (UHI) formed in the main urban
222 areas mainly due to intense solar heating under a clear and clean sky but also due to the heat
223 released by urban activities. At 12:00 LST, the warm-dry air mass driven by gusty the foehn
224 merged with the UHI, enlarging the coverage of the warm air mass. When the HF passed over
225 CDG, the pressure significantly increased (~ 0.5 hpa, Fig. 8a) as well as humidity and $PM_{2.5}$
226 concentrations, but temperature slightly decreased (Fig. 8b). CDG was also affected by the foehn
227 at around 12:00 LST, 1.5 hours later than CP, with accompanying temperature and wind speed
228 increases, and decrease in humidity.

229 At IAP around noon, a northwesterly wind and an updraft increased significantly between 450
230 m and 1250 m height above the surface, and the wind direction below 500 m changed from
231 northeast to northwest (Fig. 9). Concurrently, the tower temperatures also significantly increased
232 and relative humidity decreased, and the wind profiles changed below 320 m (Fig. 10a-b), which
233 implies IAP was affecting by the foehn at this time. The temperature increased mainly from 12:00
234 LST to 19:00 LST when turbulence also increased significantly (Fig. 10c). As the HF approached,
235 the wind weakened, the wind direction changed to southwest, and the humidity increased sharply.
236 The atmosphere became more stably stratified near the surface, leading to enhanced pollution
237 below the hundred meter level. Figure 11 shows downward shortwave radiation (DR) at IAP and
238 GXT, and $PM_{2.5}$ concentrations at AOT and YZ. Aerosols reduced the DR to 225 W m^{-2} at GXT at
239 11:00 LST, 36 W m^{-2} less than IAP. The radiation difference between IAP and GXT was 174 W m^{-2}
240 at 13:00 LST. Meanwhile, the $PM_{2.5}$ concentration was 456 $\mu\text{g m}^{-3}$ greater at YZ than ATZX.
241 At GXT, higher concentrations of aerosol particles in the polluted air mass scattered more solar
242 radiation and reduced the amount of solar radiation at the ground, leading to weaker turbulence
243 and lower PBL height which further enhanced the aerosol concentration near the ground. In
244 contrast at IAP, there were less aerosol particulates, more radiation and stronger turbulence
245 resulting in higher PBL height and less air pollutant concentration near the ground.

246 247 4 Discussion

248 The formation of the HF is illustrated in Figure 12. The fundamental process of HF formation is
249 similar to the concept of colliding density currents illustrated by Simpson (1997) and Kingsmill et



250 al. (2003), i.e., the collision of a gust front with a sea-breeze front (SBF). This results in high
251 concentrations of pollutants in the convergence zone of the front (Yoshikado et al., 1996; Dong et
252 al., 2017; Li et al., 2019). As noted by Miller et al., (2003), who described the structure and
253 characteristics of the SBF in detail, the sea breeze occurs under relatively cloud-free skies, when
254 the surface of the land heats up more rapidly than the sea. But in our case, the coastal area of
255 Bohai Bay was covered mostly by clouds, fog, and haze during the daytime (Fig. 4), which
256 decreased the contrast between the land and the sea and inhibited the sea breeze. Also, sea breezes
257 occur normally around 11:00 LST in the Bohai Bay area in winter, which is later than in summer
258 (Qiu and Fan, 2013). The typical speed of a SBF is 3.4 m s^{-1} (Simpson et al., 1977), considerably
259 larger than the observed HF speed of $\sim 0.7 \text{ m s}^{-1}$. Again, the front we studied was not a SBF;
260 nevertheless, the SBF has some similarities in shape and formation to the HF in our study. The sea
261 breeze is one example of a gravity or density current, which are primarily horizontal flows
262 generated by a density difference of only a few percent. Field studies have confirmed that the SBF,
263 as part of the sea breeze gravity current, has aspects of the sea breeze head (SBH), which had been
264 simulated by Simpson (1994, 1997) using laboratory tanks and two bodies of water of slightly
265 different densities. Likewise, in our case, a temperature difference between the warm air mass and
266 the cold air mass resulted in a density difference between these air masses. Figures S4-S7 show air
267 density distribution overlapping surface wind vectors and $\text{PM}_{2.5}$ concentrations. Note in these
268 figures that the biggest gradient of air density corresponds to the wind convergence line as well as
269 the HF line. Both the radiative heating difference between northern and southern areas, and the
270 warm and dry foehn are key factors producing warm air masses. Southern hazy air masses reflect
271 more solar radiation, and thus inhibit an increase in surface temperature and turbulence mixing,
272 leading to colder and denser air. In contrast, solar radiative heating enhances heating of the
273 northerly clear and cleaner air mass which concurrently was affected by the warm foehn, leading
274 to warmer and less dense air. The lower density air mass collides with the higher density air mass
275 and subsequently overrides the denser air mass (Fig. 1c; Fig. 5e; Fig. 12). This aspect is very
276 similar to the SBF. The warmer air overriding the cold-wet air mass also intensifies the inversion
277 at the top of the boundary between two air masses, limiting the growth rate of the underlying layer
278 and increasing its pollutant concentration. The interface between the warm-dry air mass and the
279 cold-wet air mass formed the HF and a significant convergence line at the surface. This kind of
280 convergence line can sometimes be found during air pollution events when pollutants transferred
281 by southerly winds encounter northerly mountain winds at night in the BTH region (Li et al, 2019;
282 Liang et al., 2018).

283 Typically for clear daytime conditions, the horizontal temperature differences between the air
284 over mountains and the adjacent plains can produce up-slope, up-valley, and plains-mountain
285 winds, which are usually weak and often overpowered by strong foehns (Whiteman, 2000) and
286 intensified wind speed in the upper air (Fig. 2d) as is the case here. Our results also show that the
287 pressure difference between air masses is about 0.5 hpa before and after the HF passage (Fig. 8).
288 This pressure gradient forcing creates a seesaw clash between the polluted and the clean air
289 masses. The polluted air mass repeatedly encroaches into the clean air mass and is pushed back by
290 the clean air mass. Eventually the polluted air mass wins. The lidar observed five wave-like
291 polluted air invasions (Fig. 5). Thus the pressure difference between the air masses due to different
292 air densities, although small, caused the hazy air mass to slowly swing north or northwest, and
293 inflicted severe pollution on the urban area. Li et al., 2016 showed that the polluted aerosol



294 concentration in southern Beijing is normally higher than in the urban and northern rural areas of
295 Beijing (Li et al., 2016). For typical regional air pollution events in Beijing, air pollutants are
296 mainly transported from surrounding areas, especially Hebei Province and Tianjin, south of
297 Beijing (Zheng et al., 2015; Zheng et al., 2018). Both urban heat island effects and aerosol
298 radiation forcing result in polluted areas that are colder with higher air density than less polluted
299 areas, leading to a weak pressure gradient between more polluted and less polluted air masses.
300 During the daytime, the pressure gradient forcing by air density is overlapped by the forcing of
301 plains-mountain winds, valley breezes and urban heat island circulations, enhancing air pollutant
302 transport from southern to northern areas. At night, if mountain-plains winds and mountain
303 breezes are weak, the pressure gradient forcing by air density can transport polluted air toward less
304 polluted areas, which seems not to have been discussed previously. It implies that the weak
305 pressure gradient could play an important role on air pollutants transport during the weak
306 mountain-plain wind system and mountain-valley breeze periods.

307 In order to investigate the occurrence frequency of the foehn in Beijing, we analyzed one year
308 of AWS data (PM_{2.5} data) at three sites CP (CP), AOT (AOT) and GXT (YZ), representing
309 northern suburban, urban and southern suburban areas, respectively (Table 2). For daily data
310 sampled hourly, if meteorological variables of the CP site at one hour meet the following criteria:
311 (1) one-hour temperature increase is the highest among the three sites and greater than 1.5°C and
312 at least 1.0°C higher than that at the GXT site, (2) one-hour relative humidity tendency is negative,
313 and (3) hourly wind direction is greater than 270° or less than 90°, we define this day as a foehn
314 case day. These criteria ensure that the CP site adjacent to the mountains has the most significant
315 warming among three sites with the foehn coming from the mountain and with a relative humidity
316 decrease, i.e. a typical foehn case. Note in Table 2 that during the months from OCT to MAR
317 when severe haze events are also frequent in Beijing, there is a higher foehn frequency than other
318 months. There are 16 foehn cases, about 55% of all cases, connected to air pollution events. In 10
319 cases, PM_{2.5} concentrations for all sites decreased 24 hrs after the foehn's occurrence. In 1 case,
320 PM_{2.5} concentrations for all sites increased after the foehn's occurrence. In 5 cases, including the
321 case in this article, PM_{2.5} concentrations for all sites initially decreased then increased 24 hrs after
322 the foehn's occurrence. The foehn's effects on air pollution can be direct or indirect. The direct
323 effect is that gusty foehns transport air pollutants resulting in increasing or decreasing air pollution
324 concentration depending on whether the foehns are polluted or clean. The more complicated
325 indirect effect alters air mass properties and boundary layer structure by dry and warm foehn
326 winds, which then influences air pollution. It is worth noting that type B cases in Table 2,
327 accounting for 17% of total foehn cases, are likely due to the indirect effect leading to heavier air
328 pollution, and need to be investigated further.

329

330 5 Summary and implications

331 This is the first study to our knowledge in which an HF related to the foehn in the BTH region has
332 been analyzed. Based on observations collected during SURF-15, we studied an HF on 24
333 December 2015 in Beijing. This HF was formed by the collision between a cold-humid polluted
334 air mass with higher density and a warm-dry clean air mass with lower density which was mainly
335 due to the foehn. Initially, fog occupied the plains areas southeast of Beijing associated with a
336 hazy air mass early in the morning. The hazy-foggy air mass developed and invaded Beijing
337 around noon. The fog dissipated in the afternoon. The warm-dry downslope foehn began to impact



338 the northern plains before noon and moved to the south, gradually affecting other plains sites until
339 colliding with the cold-wet polluted air mass south and east of the urban areas, leading to a
340 convergence line and the HF boundary at noon. As the HF passed by surface sites, $PM_{2.5}$
341 concentrations increased by more than $200 \mu\text{g m}^{-3}$ in 10 minutes. Following the HF, four surges of
342 polluted air invaded the IUM site and consequently produced severe pollution. The HF boundary
343 was clearly visible from satellite images and weather camera photos during the daytime. The
344 formation of the HF is very similar to the SBF, although the front in our study cannot be explained
345 as an SBF due to weak radiation and temperature contrast between the land and sea, its earlier
346 occurrence time and long distance inland. The sloped boundary of the HF tilts toward the polluted
347 air mass as a result of the warm-dry clean air mass overriding the cold-wet polluted air mass. The
348 HF slowly swings toward northern and northwestern clean areas. Our results show that as the
349 foehn wind weakened and retreated, the weak pressure gradient between the warm-dry air mass
350 and the cold-wet air mass was the main factor forcing the polluted air mass to slowly move north
351 or northwest.

352 We segregate the effect of the foehn on air pollution into two types: a direct and an indirect
353 effect. This foehn-induced HF event gives us a good opportunity to investigate both direct and
354 indirect effects of the foehn on air pollution and haze events. Some studies have revealed the
355 direct effect of the foehn on air pollution: stronger gusty foehns could diminish or even eliminate
356 air pollutants. For the seldom-studied indirect effect of the foehn, it could enhance differences in
357 radiation and air density between clean and polluted air masses, resulting in a weak pressure
358 gradient between air masses which allows the polluted air mass to invade the clean air mass. This
359 mechanism could be more dominant especially when upslope winds, valley winds, and
360 plains-mountain winds retreat after sunset in Beijing. Also, warm-dry foehns could affect urban
361 heat island and atmosphere stratification in the boundary layer, and further affect air pollution.

362 Although air pollution events in BTH region have been studied from different aspects over
363 decades, few studies have investigated the influence of the foehn on air pollution. Therefore, we
364 recommend further studies on the formation mechanism of the foehn and its effects on air
365 pollution in the BTH region.

366
367 *Data availability.* The $PM_{2.5}$ data is available on the website of Ministry of Ecology and
368 Environmental of the People's Republic of China (<http://106.37.208.233:20035>). Other data are
369 available at <http://www.iium.cn/dataCenter/> which archives the SURF filed data collected from 2015
370 and 2016.

371
372 *Author contributions.* JL, MZ had the original idea, JL, ZS, YD, ZC, YW and QL performed the
373 integrative data analysis, JL, ZS, and DL wrote the manuscript. All authors discussed the results
374 and commented on the paper.

375
376 *Competing interests.* The authors declare that they have no conflict of interest.

377
378 *Acknowledgments.* The authors would like thank the anonymous reviewers for their helpful
379 comments. This work was supported by the National Natural Science Foundation of China
380 (41875123); the Ministry of Science and Technology of China (Grant No. 2016YFC0203302);
381 Beijing Natural Science Foundation of China (8171002). This material is based upon work



382 supported by the National Center for Atmospheric Research, which is a major facility sponsored
383 by the National Science Foundation under Cooperative Agreement No. 1852977.
384
385
386



- 387 References
- 388 Ahrens C. D.: *Meteorology Today: An Introduction to Weather, Climate and the Environment*. Thomson Learning,
- 389 USA, 2003.
- 390 Brinkmann, W.: What is a foehn?, *Weather*, 26, 230–239, doi:10.1002/j.1477-8696.1971.tb04200.x., 1971.
- 391 Chen, J., Li, Z., Lv, M., Wang, Y., Wang, W., Zhang, Y., Wang, H., Yan, X., Sun, Y., and Cribb, M.: Aerosol
- 392 hygroscopic growth, contributing factors, and impact on haze events in a severely polluted region in northern
- 393 China, *Atmos. Chem. Phys.*, 19, 1327–1342, <https://doi.org/10.5194/acp-19-1327-2019>, 2019.
- 394 Dang, R. and Liao, H.: Severe winter haze days in the Beijing–Tianjin–Hebei region from 1985 to 2017 and the
- 395 roles of anthropogenic emissions and meteorology, *Atmos. Chem. Phys.*, 19, 10801–10816,
- 396 <https://doi.org/10.5194/acp-19-10801-2019>, 2019.
- 397 Dong G., Y. L., Hao T.: Analysis of meteorological characteristics of heavy haze process in Tianjin in autumn and
- 398 winter and the role of sea breeze, *Environmental Science & Technology*, 40, 117–123,
- 399 <https://doi.org/10.3969/j.issn.1003-6504.2017.10.020>, 2017 (in Chinese).
- 400 Drechsel S, Mayr J.: Objective forecasting of Foehn winds for a subgrid-scale Alpine Valley, *Weather Forecast*
- 401 23:205–218. <https://doi.org/10.1175/2007WAF021.1>, 2008.
- 402 Elvidge, A. D., and Renfrew, I. A.: The Causes of Foehn Warming in the Lee of Mountains, *Bulletin of the*
- 403 *American Meteorological Society*, 97, 455–466, <https://doi.org/10.1175/bams-d-14-00194.1>, 2016.
- 404 Gao, Y., Zhang, M., Liu, Z., Wang, L., Wang, P., Xia, X., Tao, M., and Zhu, L.: Modeling the feedback between
- 405 aerosol and meteorological variables in the atmospheric boundary layer during a severe fog–haze event over the
- 406 North China Plain, *Atmos. Chem. Phys.*, 15, 4279–4295, <https://doi.org/10.5194/acp-15-4279-2015>, 2015.
- 407 Gohm, A., Harnisch, F., Vergeiner, J., Obleitner, F., Schnitzhofer, R., Hansel, A., Fix, A., Neiniger, B., Emeis, S.,
- 408 and Schafer, K.: Air pollution transport in an Alpine valley: Results from airborne and ground-based
- 409 observations, *Boundary-Layer Meteorol.*, 131, 441–463, <https://doi.org/10.1007/s10546-009-9371-9>, 2009.
- 410 Guo, H., Cheng, T., Gu, X., Wang, Y., Chen, H., Bao, F., Shi, S., Xu, B., Wang, W., Zuo, X., Zhang, X., and
- 411 Meng, C.: Assessment of PM_{2.5} concentrations and exposure throughout China using ground observations, *Sci.*
- 412 *Total Environ.*, 601–602, 1024–1030, <https://doi.org/10.1016/j.scitotenv.2017.05.263>, 2017.
- 413 Han, S., Hao, T., Zhang, Y., Liu, J., Li, P., Cai, Z., Zhang, M., Wang, Q., and Zhang, H.: Vertical observation and
- 414 analysis on rapid formation and evolutionary mechanisms of a prolonged haze episode over Central-Eastern
- 415 China, *Sci. Total Environ.*, 616–617, 135–146, <https://doi.org/10.1016/j.scitotenv.2017.10.278>, 2018.
- 416 Han, T., Liu, X., Zhang, Y., Qu, Y., Zeng, L., Hu, M., and Zhu, T.: Role of secondary aerosols in haze formation
- 417 in summer in the Megacity Beijing, *J. Environ. Sci.*, 31, 51–60, <https://doi.org/10.1016/j.jes.2014.08.026>, 2015.
- 418 Han, X., Zhang, M., Gao, J., Wang, S., and Chai, F.: Modeling analysis of the seasonal characteristics of haze
- 419 formation in Beijing, *Atmos. Chem. Phys.*, 14, 10231–10248, <https://doi.org/10.5194/acp-14-10231-2014>,
- 420 2014.
- 421 Huang, R. J., Zhang, Y., Bozzetti, C., Ho, K. F., Cao, J. J., Han, Y., Daellenbach, K. R., Slowik, J. G., Platt, S. M.,
- 422 Canonaco, F., Zotter, P., Wolf, R., Pieber, S. M., Brun, E. A., Crippa, M., Ciarelli, G., Piazzalunga, A.,
- 423 Schwikowski, M., Abbaszade, G., Schnelle-Kreis, J., Zimmermann, R., An, Z., Szidat, S., Baltensperger, U., El
- 424 Haddad, I., and Prevot, A. S.: High secondary aerosol contribution to particulate pollution during haze events in
- 425 China, *Nature*, 514, 218–222, <https://doi.org/10.1038/nature13774>, 2014.
- 426 Huang, X., Wang, Z., and Ding, A.: Impact of Aerosol-PBL Interaction on Haze Pollution: Multiyear
- 427 Observational Evidences in North China, *Geophys. Res. Lett.*, 45, 8596–8603,
- 428 <https://doi.org/10.1029/2018gl079239>, 2018.
- 429 Jiang, J. K., Zhou, W., Cheng, Z., Wang, S. X., He, K. B., and Hao, J. M.: Particulate Matter Distributions in
- 430 China during a Winter Period with Frequent Pollution Episodes (January 2013), *Aerosol Air Qual. Res.*, 15,



- 431 494–503, <https://doi.org/10.4209/aaqr.2014.04.0070>, 2015a.
- 432 Jiang, C., Wang, H., Zhao, T., Li, T., and Che, H.: Modeling study of PM_{2.5} pollutant transport across cities in
433 China's Jing–Jin–Ji region during a severe haze episode in December 2013, *Atmos. Chem. Phys.*, 15,
434 5803–5814, <https://doi.org/10.5194/acp-15-5803-2015>, 2015b.
- 435 Kingsmill, D. E. and Crook N. A.: An observational study of atmospheric bore formation from colliding density
436 currents, *Monthly Weather Review*, 131, 2985–3002,
437 [https://doi.org/10.1175/1520-0493\(2003\)131<2985:Aosob>2.0.Co;2..2003](https://doi.org/10.1175/1520-0493(2003)131<2985:Aosob>2.0.Co;2..2003).
- 438 Li, K., Liao, H., Cai, W., and Yang, Y.: Attribution of Anthropogenic Influence on Atmospheric Patterns
439 Conducive to Recent Most Severe Haze Over Eastern China, *Geophys. Res. Lett.*, 45, 2072–2081,
440 <https://doi.org/10.1002/2017gl076570>, 2018a.
- 441 Li, J., Sun, J., Zhou, M., Cheng, Z., Li, Q., Cao, X., Zhang, J.: Observational analyses of dramatic developments of
442 a severe air pollution event in the Beijing area, *Atmos. Chem. Phys.*, 18 (6), 3919–3935,
443 <https://doi.org/10.5194/acp-2017-909>, 2018b.
- 444 Li Q., L. J., Zheng Z., Wang Y., Yu M.: Influence of Mountain Valley Breeze and Sea Land Breeze in Winter on
445 Distribution of Air Pollutants in Beijing-Tianjin-Hebei Region, *Environmental Science*, 40, 513–524,
446 <https://doi.org/10.13227/j.hjxk.201803193>, 2019 (in Chinese).
- 447 Li, J., Du, H., Wang, Z., Sun, Y., Yang, W., Li, J., Tang, X., and Fu, P.: Rapid formation of a severe regional
448 winter haze episode over a mega-city cluster on the North China Plain, *Environ. Pollut.*, 223, 605–615,
449 <https://doi.org/10.1016/j.envpol.2017.01.063>, 2017.
- 450 Li, L., Wang, Z., Zhang, D., Chen, T., Jiang, L., and Li, Y.: Analysis of heavy air pollution episodes in Beijing
451 during 2013–2014, *Chinese Environmental Science*, 36, 27–35, 2016 (in Chinese).
- 452 Li, X., Xia, X., Wang, L., Cai, R., Zhao, L., Feng, Z., Ren, Q., Zhao, K.: The role of foehn in the formation of
453 heavy air pollution events in Urumqi, China. *J. Geophys. Res. Atmos.*, 120, 5371–5384,
454 <https://doi.org/10.1002/2014jd022778>, 2015.
- 455 Liang, X., Miao, S., Li, J., Bornstein, R., Zhang, X., Gao, Y., Cao, X., Chen, F., Cheng, Z., Clements, C., Debberdt,
456 W., Ding, A., Ding, D., Dou, J. J., Dou, J. X., Dou, Y., Grimoond, C. S. B., Gonzalez-Cruz, J., He, J., Huang,
457 M., Huang, X., Ju, S., Li, Q., Niyogi, D., Quan, J., Sun, J., Sun, J. Z., Yu, M., Zhang, J., Zhang, Y., Zhao, X.,
458 Zheng, Z., and Zhou, M.: SURF: Understanding and predicting urban convection and haze, *Bulletin of the
459 American Meteorological Society*, 99(7): 1391–1413, <https://doi.org/10.1175/bams-d-16-0178.1>, 2018.
- 460 Liu, Q., Jia, X., Quan, J., Li, J., Li, X., Wu, Y., Chen, D., Wang, Z., and Liu, Y.: New positive feedback
461 mechanism between boundary layer meteorology and secondary aerosol formation during severe haze events,
462 *Sci. Rep.*, 8, 6095, <https://doi.org/10.1038/s41598-018-24366-3>, 2018.
- 463 Liu, S., Liu, Z., Li, J., Wang, Y., Ma, Y., Sheng, L., Liu, H., Liang, F., Xin, G., and Wang, J.: Numerical
464 simulation for the coupling effect of local atmospheric circulations over the area of Beijing, Tianjin and Hebei
465 province, *Sci. China Ser. D*, 52, 382–392, <https://doi.org/10.1007/s11430-009-0030-2>, 2009.
- 466 Liu, T., Gong, S., He, J., Yu, M., Wang, Q., Li, H., Liu, W., Zhang, J., Li, L., Wang, X., Li, S., Lu, Y., Du, H.,
467 Wang, Y., Zhou, C., Liu, H., and Zhao, Q.: Attributions of meteorological and emission factors to the 2015
468 winter severe haze pollution episodes in China's Jing-Jin-Ji area, *Atmos. Chem. Phys.*, 17, 2971–2980,
469 <https://doi.org/10.5194/acp-17-2971-2017>, 2017.
- 470 Liu, X. G., Li, J., Qu, Y., Han, T., Hou, L., Gu, J., Chen, C., Yang, Y., Liu, X., Yang, T., Zhang, Y., Tian, H., and
471 Hu, M.: Formation and evolution mechanism of regional haze: a case study in the megacity Beijing, China,
472 *Atmos. Chem. Phys.*, 13, 4501–4514, <https://doi.org/10.5194/acp-13-4501-2013>, 2013.
- 473 Luo R., Zheng Y G., Chen M.: Mechanism of a rare night sudden intense warming event in Beijing and
474 surrounding area. *Meteorological Monthly*, 46, 478–489, 2020 (in Chinese).



- 475 Ma, Q., Wu, Y., Zhang, D., Wang, X., Xia, Y., Liu, X., Tian, P., Han, Z., Xia, X., Wang, Y., and Zhang, R.: Roles
476 of regional transport and heterogeneous reactions in the PM_{2.5} increase during winter haze episodes in Beijing,
477 *Sci. Total Environ.*, 599–600, 246–253, <https://doi.org/10.1016/j.scitotenv.2017.04.193>, 2017.
- 478 McGowan, H. A., A. P. Sturman, M. Kossmann, and P. Zawar-Reza : Observation of foehn onset in the Southern
479 Alps, New Zealand, *Meteorol. Atmos. Phys.*, 79, 215–230, <https://doi.org/10.1007/s007030200004>, 2002.
- 480 McGowan, H. A., P. A. Sturman, and F. L. Owens : Aeolian dust transport and deposition by foehn winds in an
481 alpine environment, Lake Tekapo, New Zealand, *Geomorphology*, 15(2), 135–146,
482 [https://doi.org/10.1016/0169-555X\(95\)00123-M](https://doi.org/10.1016/0169-555X(95)00123-M), 1996.
- 483 Miao, Y., J. Guo, S. Liu, H. Liu, G. Zhang, Y. Yan, and J. He: Relay transport of aerosols to Beijing-Tianjin-Hebei
484 region by multi-scale atmospheric circulations. *Atmospheric Environment*, 165, 35–45,
485 <https://doi.org/10.1016/j.atmosenv.2017.06.032>, 2017.
- 486 Miller, S. T. K., Keim B. D., Talbot R. W., and Mao H.: Sea breeze: Structure, forecasting, and impacts. *Reviews*
487 *of Geophysics*, 41(3), 1–31, <https://doi.org/10.1029/2003rg000124>, 2003.
- 488 Nkemdirim LC., Leggat K.: The effect of Chinook weather on urban heat islands and air pollution. *Water Air Soil*
489 *Pollut* 9:53–67, 1978.
- 490 Norte, F.: Understanding and Forecasting Zonda Wind (Andean Foehn) in Argentina: A Review. *Atmospheric and*
491 *Climate Sciences*, 5, 163–193. <https://doi.org/10.4236/acs.2015.53012>, 2015.
- 492 Pet ä ä T., Järvi, L., Kerminen, V.-M., Ding, A.J., Sun, J.N., Nie, W., Kujansuu, J., Virkkula, A., Yang, X., Fu,
493 C.B., Zilitinkevich, S., Kulmala, M.: Enhanced air pollution via aerosol-boundary layer feedback in China. *Sci.*
494 *Rep.* 6, 18998, <https://doi.org/10.1038/srep18998>, 2016.
- 495 Qiu X., Fang. S.: Progress of Sea-Land Breeze Study and Characteristics of Sea-Land Breeze in Three Coastal
496 Areas in China, *Meteorological Monthly*, 39, 186–193, <https://doi.org/10.7519/j.issn.1000-0526.2013.02.007>,
497 2013 (in Chinese).
- 498 Ren, Y., Zhang, H., Wei, W., Wu, B., Cai, X., and Song, Y.: Effects of turbulence structure and urbanization on
499 the heavy haze pollution process, *Atmos. Chem. Phys.*, 19, 1041–1057,
500 <https://doi.org/10.5194/acp-19-1041-2019>, 2019.
- 501 Richner, H. and H ä hler, P.: Understanding and forecasting Alpine foehn, in *Mountain Weather Research and*
502 *Forecasting*, Springer Atmospheric Sciences, edited by F. K. Chow, S. F. J. De Walker, and B. J. Snyder, pp.
503 219–260, Springer, Netherlands, 2013.
- 504 Simpson, J. E., D. A. Mansfield, and J. R. Milford, Inland penetration of sea-breeze fronts, *Q. J. R. Meteorol. Soc.*,
505 103,47–76, 1977.
- 506 Simpson, J. E., *Gravity Currents in the Environment and the Laboratory*, 244 pp., Cambridge Univ. Press, New
507 York, 1997.
- 508 Simpson, J. E., *Sea Breeze and Local Wind*, 234 pp., Cambridge Univ. Press, New York, 1994.
- 509 Steiner, A. L., Mermelstein, D., Cheng, S. J., Twine, T. E., and Oliphant, A.: Observed Impact of Atmospheric
510 Aerosols on the Surface Energy Budget, *Earth Interact.*, 17, 1–22, <https://doi.org/10.1175/2013ei000523.1>,
511 2013.
- 512 Su, T., Li, Z., and Kahn, R.: Relationships between the planetary boundary layer height and surface pollutants
513 derived from lidar observations over China: regional pattern and influencing factors, *Atmos. Chem. Phys.*, 18,
514 15921–15935, <https://doi.org/10.5194/acp-18-15921-2018>, 2018.
- 515 Sun, F., Zhang, D., Sun, R., Dong, X., Wang, X., Wang, Z., and Cheng, N.: Typical heavy pollution episode
516 analysis on PM_{2.5} in winter of Beijing, *Environment Monitoring in China*, 30, 1–12,
517 <https://doi.org/10.3969/j.issn.1002-6002.2014.06.001>, 2014 (in Chinese).
- 518 Sun, Y. L., Jiang, Q., Wang, Z. F., Fu, P. Q., Li, J., Yang, T., and Yin, Y.: Investigation of the sources and



- 519 evolution processes of severe haze pollution in Beijing in January 2013, *J. Geophys. Res.-Atmos.*, 119,
520 4380–4398, <https://doi.org/10.1002/2014jd021641>, 2014.
- 521 Sun, Y., Chen, C., Zhang, Y., Xu, W., Zhou, L., Cheng, X., Zheng, H., Ji, D., Li, J., Tang, X., Fu, P., and Wang, Z.:
522 Rapid formation and evolution of an extreme haze episode in Northern China during winter 2015, *Sci. Rep.*, 6,
523 27151, <https://doi.org/10.1038/srep27151>, 2016.
- 524 Takane, Y. and Kusaka H.: Formation Mechanisms of the Extreme High Surface Air Temperature of 40.9 °C
525 Observed in the Tokyo Metropolitan Area: Considerations of Dynamic Foehn and Foehnlike Wind. *J. Appl.*
526 *Meteor. Climatol.*, 50, 1827–1841, <https://doi.org/10.1175/JAMC-D-10-05032.1>, 2011.
- 527 Tie, X., Huang, R.-J., Cao, J., Zhang, Q., Cheng, Y., Su, H., Chang, D., Pöschl, U., Hoffmann, T., Dusek, U., Li,
528 G., Worsnop, D. R., and O'Dowd, C. D.: Severe Pollution in China Amplified by Atmospheric Moisture, *Sci.*
529 *Rep.-UK*, 7, 15760, <https://doi.org/10.1038/s41598-017-15909-1>, 2017.
- 530 Vergeiner, J. : South foehn studies and a new foehn classification scheme in the Wipp and Inn Valley, PhD thesis,
531 Univ. of Innsbruck, Austria, 2004.
- 532 Wang, Z., Ding, Y., Zhang, Y., Wang, C., Li J., Gu, Y.: Feature and Mechanism of the Foehn Weather on East
533 Slope Taihang Mountains I :Statistic Feature. *PLATEAU METEOROLOGY*, 31, 547-554, 2012a (in Chinese).
- 534 Wang, Z., Ding, Y., Zhang, Y., Fan, J., Zhang, S., Tian L.: Feature and Mechanism of the Foehn Weather on East
535 Slope Taihang Mountains II :Case Analysis of the Effects of Lee Wave on Foehn Occurring and Moving, 31,
536 555-561, 2012b (in Chinese).
- 537 Wang, Y. H., Liu, Z. R., Zhang, J. K., Hu, B., Ji, D. S., Yu, Y. C., and Wang, Y. S.: Aerosol physicochemical
538 properties and implications for visibility during an intense haze episode during winter in Beijing, *Atmos. Chem.*
539 *Phys.*, 15, 3205–3215, <https://doi.org/10.5194/acp-15-3205-2015>, 2015.
- 540 Wang, Y., Bao, S., Wang, S., Hu, Y., Shi, X., Wang, J., Zhao, B., Jiang, J., Zheng, M., Wu, M., Ruseel, A., Wang,
541 Y., and Hao, J.: Local and regional contributions to fine particulate matter in Beijing during heavy haze
542 episodes, *Sci. Total Environ.*, 580, 283–296, <https://doi.org/10.1016/j.scitotenv.2016.12.127>, 2017.
- 543 Wang, Y., Yao, L., Wang, L., Liu, Z., Ji, D., Tang, G., Zhang, J., Sun, Y., Hu, B., and Xin, J.: Mechanism for the
544 formation of the January 2013 heavy haze pollution episode over central and eastern China, *Science China*
545 *Earth Sciences*, 57, 14–25, <https://doi.org/10.1007/s11430-013-4773-4>, 2013.
- 546 Whiteman, C. D.: *Mountain Meteorology: Fundamentals and Applications*, Oxford Univ. Press, New York, 2000.
- 547 Wu, J., Bei, N., Hu, B., Liu, S., Zhou, M., Wang, Q., Li, X., Liu, L., Feng, T., Liu, Z., Wang, Y., Cao, J., Tie, X.,
548 Wang, J., Molina, L. T., and Li, G.: Is water vapor a key player of the wintertime haze in North China Plain?,
549 *Atmos. Chem. Phys.*, 19, 8721–8739, <https://doi.org/10.5194/acp-19-8721-2019>, 2019.
- 550 Yang Xiaoliang, Y. M., Li Jiangbo, Zhang Shan: Impact Analysis of a Taihang Mountain Fohn on Haze Intensity.
551 *Meteorological Monthly*, 44, 313-319, <https://doi.org/10.7519/j.issn.1000-0526.2018.02.011>, 2018.
- 552 Yoshikado Hiroshi and Tsuchida Makoto: High levels of winter air pollution under the influence of the urban heat
553 island along the shore of Tokyo Bay, *Journal of Applied Meteorology*, 35, 1804-1813, 1996.
- 554 Zhang, B., Wang, Y., and Hao, J.: Simulating aerosol–radiation–cloud feedbacks on meteorology and air quality
555 over eastern China under severe haze conditions in winter, *Atmos. Chem. Phys.*, 15, 2387–2404,
556 <https://doi.org/10.5194/acp-15-2387-2015>, 2015.
- 557 Zhang, R. H., Li, Q., and Zhang, R. N.: Meteorological conditions for the persistent severe fog and haze event over
558 eastern China in January 2013, *Sci. China Earth Sci.*, 57, 26–35, <https://doi.org/10.1007/s11430-013-4774-3>,
559 2014.
- 560 Zhao, S., W. R., Guo Yanbo, Tan Jianlong, Shi Zhizeng: The Foehn in the Middle Range of Taihang Mountain.
561 *Meteorological Monthly*, 19, 3-6, <https://doi.org/10.7519/j.issn.1000-0526.1993.2.001>, 1993 (in Chinese).
- 562 Zhao, X. J., Zhao, P. S., Xu, J., Meng, W., Pu, W. W., Dong, F. He, D., and Shi, Q. F.: Analysis of a winter



- 563 regional haze event and its formation mechanism in the North China Plain, *Atmos. Chem. Phys.*, 13,
564 5685–5696, <https://doi.org/10.5194/acp-13-5685-2013>, 2013.
- 565 Zheng, G. J., Duan, F. K., Su, H., Ma, Y. L., Cheng, Y., Zheng, B., Zhang, Q., Huang, T., Kimoto, T., Chang, D.,
566 Pöschl, U., Cheng, Y. F., and He, K. B.: Exploring the severe winter haze in Beijing: the impact of synoptic
567 weather, regional transport and heterogeneous reactions, *Atmos. Chem. Phys.*, 15, 2969–2983,
568 <https://doi.org/10.5194/acp-15-2969-2015>, 2015.
- 569 Zhong, J., Zhang, X., Wang, Y., Sun, J., Zhang, Y., Wang, J., Tan, K., Shen, X., Che, H., Zhang, L., Zhang, Z., Qi,
570 X., Zhao, H., Ren, S., and Li, Y.: Relative contributions of boundary layer meteorological factors to the
571 explosive growth of PM_{2.5} during the red-alert heavy pollution episodes in Beijing in December 2016, *J.*
572 *Meteorol. Res.-PRC*, 31, 809–819, <https://doi.org/10.1007/s13351-017-7088-0>, 2017.
- 573 Zheng, Z., Xu, G., Yang, Y., Wang, Y., Li, Q.: Statistical characteristics and the urban spillover effect of haze
574 pollution in the circum-Beijing region, *Atmos. Pollut. Res.* 9, 1062–1071,
575 <https://doi.org/10.1016/j.apr.2018.04.004>, 2018.
- 576



577 **Table 1.** Latitude, longitude, altitude, site type and instrumentation at the main sites in Fig.1.

Site name	Latitude	Longitude	Altitude (m MSL)	Site type	Instrumentation
GXT	39.806	116.469	31	Meteorology	radiosonde, radiometer, wind profiler, AWS, pyranometer
IAP	39.974	116.371	29	Meteorology	325-m tower, sonic anemometers, doppler lidar, vertical scanning MPL, pyrgeometer and pyranometer
IUM	39.95	116.28	37	Meteorology	PPI scanning MPL, weather camera, particulates sampler and analyzer
CDG	39.945	116.291	58	Meteorology	AWS
CP	40.223	116.212	76	Meteorology & Air quality	AWS, particulates sampler and analyzer
HD	39.987	116.291	46	Meteorology	AWS, wind profiler
AOT	39.982	116.397	–	Meteorology & Air quality	particulates sampler and analyzer
YZ	39.795	116.506	–	Air quality	particulates sampler and analyzer

578

579

× AWS: automated weather station; MPL: micro pulse lidar; PPI: plain position indicator

580

581

582



583 **Table 2.** Number of foehn cases in Beijing from 1 March 2015 to 29 February 2016

	JAN	FEB	MAR	APR	MAY	JUN	JUL	AUG	SEP	OCT	NOV	DEC	Total cases
Clean cases	4	2	1	0	1	1	0	1	0	2	1	0	13
Polluted cases	Type A	1	2	2	0	1	0	0	0	2	0	2	10
	Type B	1	0	1	0	0	0	0	0	0	1	2	5
	Type C	0	0	0	0	0	0	0	1	0	0	0	1
All cases	6	4	4	0	2	1	0	1	1	4	2	4	29

584 Clean cases: foehn cases in which average $PM_{2.5}$ concentrations for CP, AOT and YZ is less than $50 \mu\text{g m}^{-3}$.

585 Polluted cases: foehn cases in average $PM_{2.5}$ concentrations for CP, AOT and YZ is greater than $50 \mu\text{g m}^{-3}$.

586 Type A: polluted cases with $PM_{2.5}$ concentrations for CP, AOT and YZ sites decreasing since foehn's occurrence in 24 hours.

587 Type B: polluted cases with $PM_{2.5}$ concentrations for CP, AOT and YZ sites initially decreasing then increasing since foehn's occurrence in 24 hours.

589 Type C: polluted cases but $PM_{2.5}$ concentrations for CP, AOT and YZ sites increasing since foehn's occurrence in 24 hours.

590 All cases: all of clean cases and polluted cases.

591

592

593

594

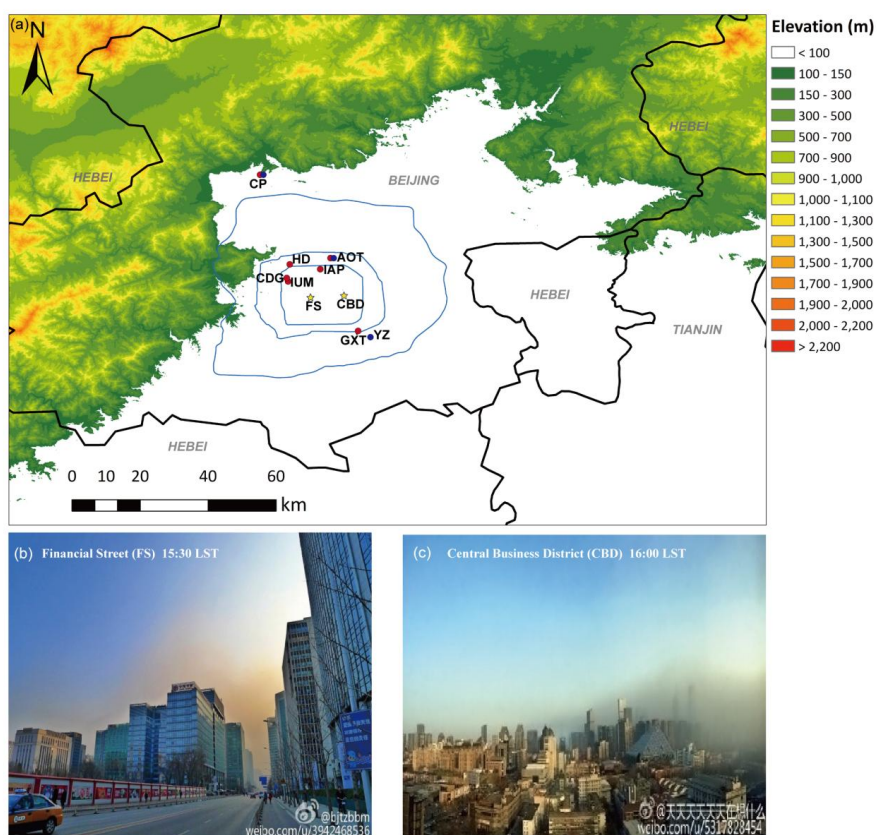
595



- 596 Figure Captions
- 597 Figure 1. (a) Locations of main observational stations (red dots: meteorological stations; blue dots:
- 598 air quality monitoring stations) used here, along with the fourth, fifth and sixth ring
- 599 roads (blue lines) in Beijing, China. Anonymous photos from SINA Weibo (like Twitter
- 600 but in Chinese) at (b) Financial Street (FS) at 15:30 and (c) Central Business District
- 601 (CBD) at 16:00 on 24 December 2015. Locations for taking the photos are shown as
- 602 yellow stars in the upper map.
- 603 Figure 2. (a) Hourly-mean PM_{2.5} concentration of 35 air quality stations in Beijing from 23
- 604 December to 25 December. Temperature (solid), dew point (dashed), and wind vectors
- 605 (in knots) from the radio sounding profiles at (b) 00:00 UTC and (c) 12:00 UTC at GXT.
- 606 (d) The temporal variation of hourly wind-vector profiles from the wind profiler at HD
- 607 on 24 December 2015.
- 608 Figure 3. The 500 mb weather maps at (a) 08:00 LST and (b) 20:00 LST, the 800 mb weather
- 609 maps at (c) 08:00 LST and (d) 20:00 LST, and surface maps at (e) 08:00 LST and (f)
- 610 20:00 LST on 24 December 2015.
- 611 Figure 4. Cloud images from the visible channels of the Himawari satellite at (a) 08:00 LST, (b)
- 612 10:00 LST, (c) 12:00 LST, (d) 14:00 LST, (e) 15:00 LST, and (f) 16:00 LST on 24
- 613 December 2015. Red, yellow and blue dots are the locations of IUM, IAP and GXT,
- 614 respectively.
- 615 Figure 5. (a) The Min-MPL vertically scanned normalized relative backscatter (NRB) at IAP
- 616 station. (b) 5-min average wind speed (red line), wind direction (triangles) at CDG
- 617 station and PM_{2.5} concentrations (blue line) at IUM station. (c) The NRB from a
- 618 Min-MPL at IAP scanning in (d) plan position indicator (PPI) mode using 10°
- 619 horizontal angle intervals from 340° to 220° and with the elevation angle at 5°. (e) Four
- 620 photos taken by the weather camera at IUM at times t₁, t₂, t₃ and t₄ which are marked
- 621 as red lines in the upper plot.
- 622 Figure 6. Temperature (color filled dots coded according to the bottom color bar), wind vectors (2
- 623 m s⁻¹ is one full bar) and PM_{2.5} concentrations (purple circles; the size of the circle
- 624 represents concentration values) in the plain area within and around Beijing at (a) 12:00
- 625 LST and (b) 16:00 LST. The blue lines indicate the location of the haze front.
- 626 Figure 7. Same as Fig 6, but with relative humidity.
- 627 Figure 8. Three-hourly (a) pressure tendency, (b) air temperature tendency, and (c) specific
- 628 humidity, (d) wind speed (lines) and wind directions (colored dots), and (e) PM_{2.5}
- 629 concentration at CP (red line), CDG (blue dash line) and GXT (black dash line) on 24
- 630 December 2015.
- 631 Figure 9. Doppler lidar observations of (a) vertical wind velocity, (b) horizontal wind speed, (c)
- 632 wind direction, and (d) carrier-noise-ratio (CNR) at IAP on 24 December 2015.
- 633 Figure 10. Temporal variations of (a) temperature (colored contours) and wind vectors, (b) relative
- 634 humidity (colored contours) and wind vectors at 15 levels on the IAP tower, and (c)
- 635 vertical velocity variance at 47 m and 280 m on the IAP tower on 24 December 2015.
- 636 Figure 11. The temporal variations of PM_{2.5} concentrations at ATZX (blue bars) and YZ (red
- 637 bars), and downward short-wave radiation at GXT and at heights of 47 m, 140 m and
- 638 280 m at the IAP tower during daytime on 24 December 2015.
- 639 Figure 12. Schematic diagram of the haze front formation.



640



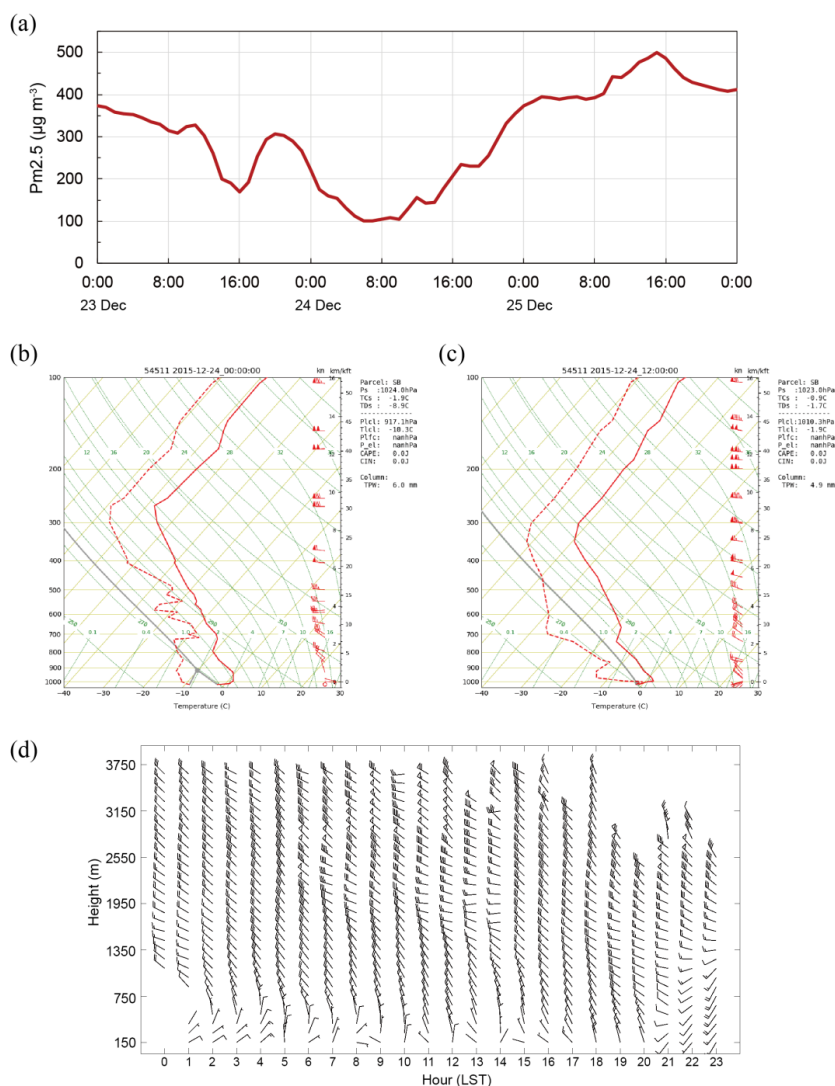
641

642

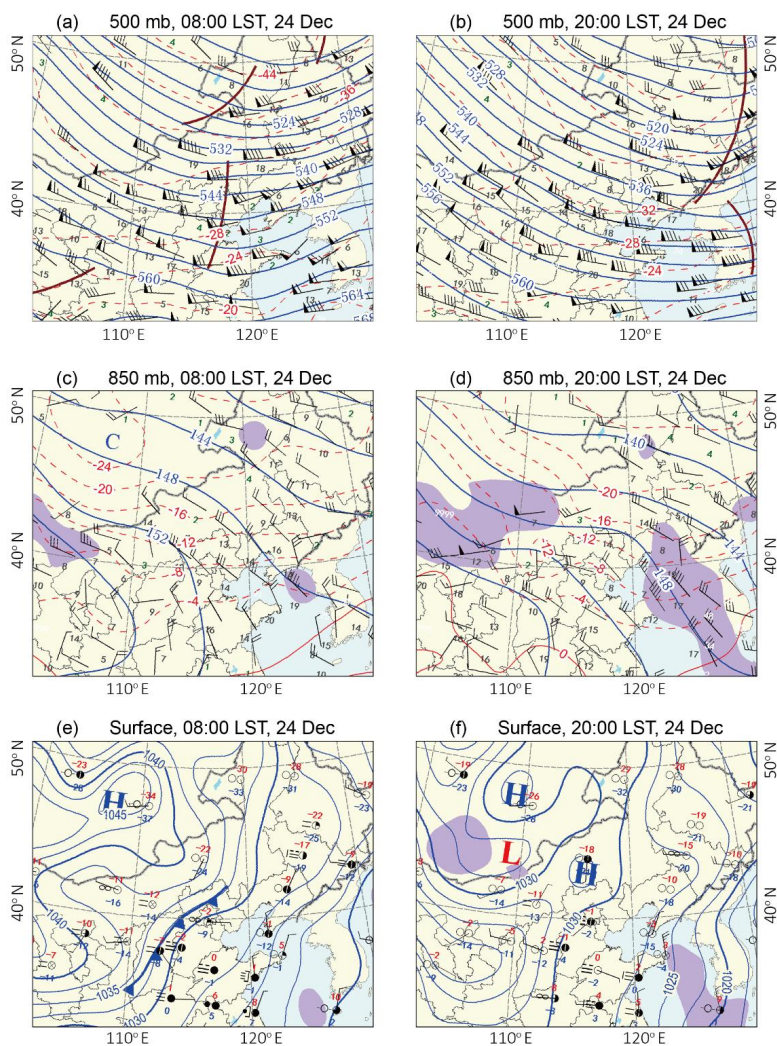
643 Figure 1. (a) Locations of main observational stations (red dots: meteorological stations; blue dots:
644 air quality monitoring stations) used here, along with the fourth, fifth and sixth ring roads (blue
645 lines) in Beijing, China. Anonymous photos from SINA Weibo (like Twitter but in Chinese) at (b)
646 Financial Street (FS) at 15:30 and (c) Central Business District (CBD) at 16:00 on 24 December
647 2015. Locations for taking the photos are shown as yellow stars in the upper map.

648

649

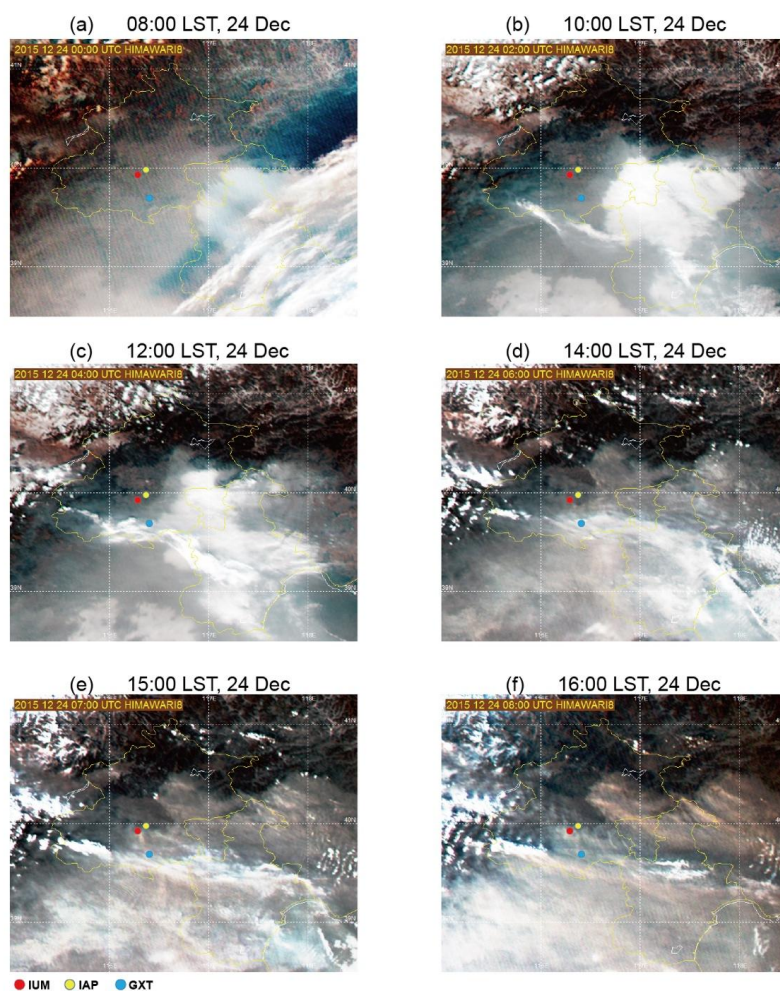


650
651 Figure 2. (a) Hourly-mean PM_{2.5} concentration of 35 air quality stations in Beijing from 23
652 December to 25 December. Temperature (solid), dew point (dashed), and wind vectors (in knots)
653 from the radio sounding profiles at (b) 00:00 UTC and (c) 12:00 UTC at GXT. (d) The temporal
654 variation of hourly wind-vector profiles from the wind profiler at HD on 24 December 2015.
655
656
657

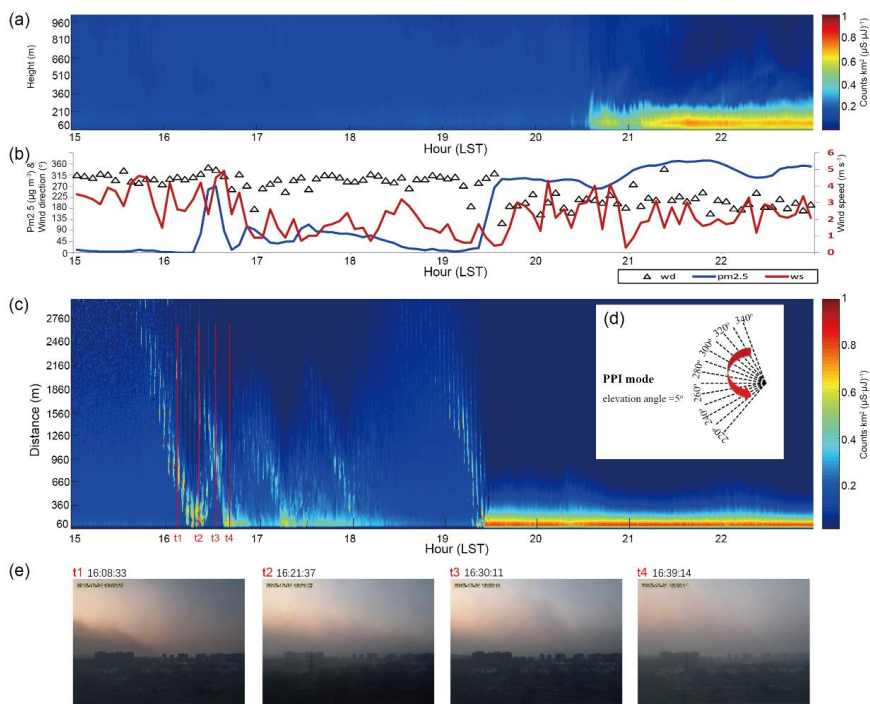


658

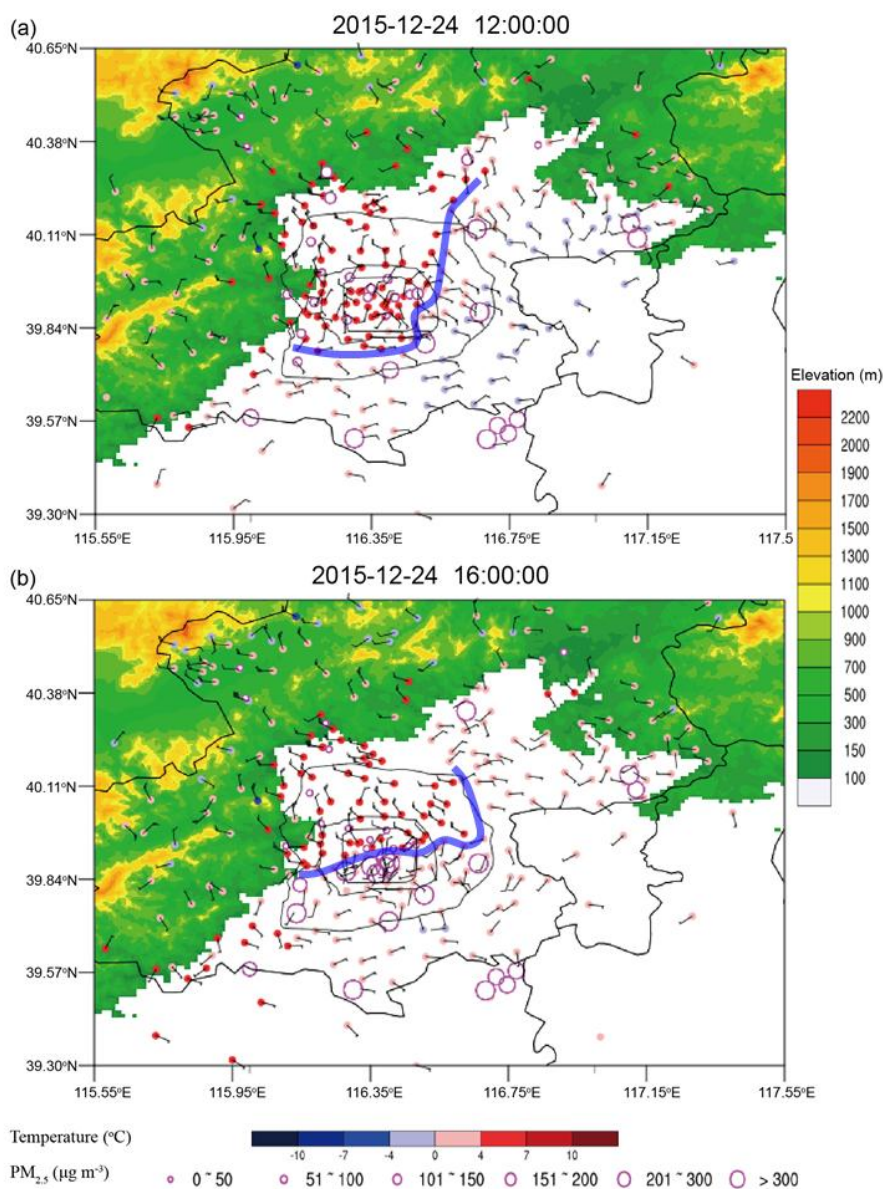
659 Figure 3. The 500 mb weather maps at (a) 08:00 LST and (b) 20:00 LST, the 800 mb weather
660 maps at (c) 08:00 LST and (d) 20:00 LST, and surface maps at (e) 08:00 LST and (f) 20:00 LST
661 on 24 December 2015.



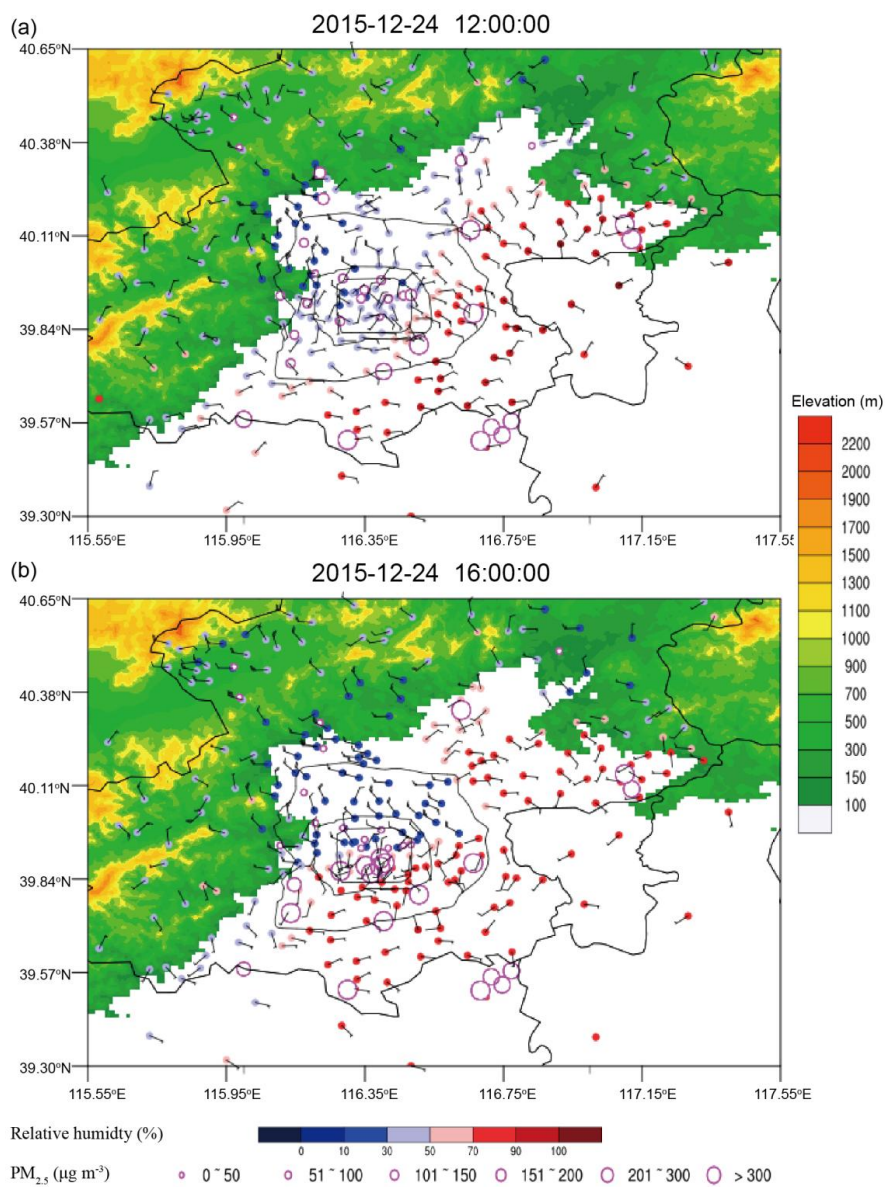
662
663 Figure 4. Cloud images from the visible channels of the Himawari satellite at (a) 08:00 LST, (b)
664 10:00 LST, (c) 12:00 LST, (d) 14:00 LST, (e) 15:00 LST, and (f) 16:00 LST on 24 December 2015.
665 Red, yellow and blue dots are the locations of IUM, IAP and GXT, respectively.
666
667
668
669



670
671 Figure 5. (a) The Min-MPL vertically scanned normalized relative backscatter (NRB) at IAP
672 station. (b) 5-min average wind speed (red line), wind direction (triangles) at CDG station and
673 PM_{2.5} concentrations (blue line) at IUM station. (c) The NRB from a Min-MPL at IAP scanning in
674 (d) plan position indicator (PPI) mode using 10° horizontal angle intervals from 340° to 220° and
675 with the elevation angle at 5°. (e) Four photos taken by the weather camera at IUM at times t1, t2,
676 t3 and t4 which are marked as red lines in the upper plot.
677



678
679 Figure 6. Temperature (color filled dots coded according to the bottom color bar), wind vectors (2
680 m s⁻¹ is one full bar) and PM_{2.5} concentrations (purple circles; the size of the circle represents
681 concentration values) in the plain area within and around Beijing at (a) 12:00 LST and (b) 16:00
682 LST. The blue lines indicate the location of the haze front.



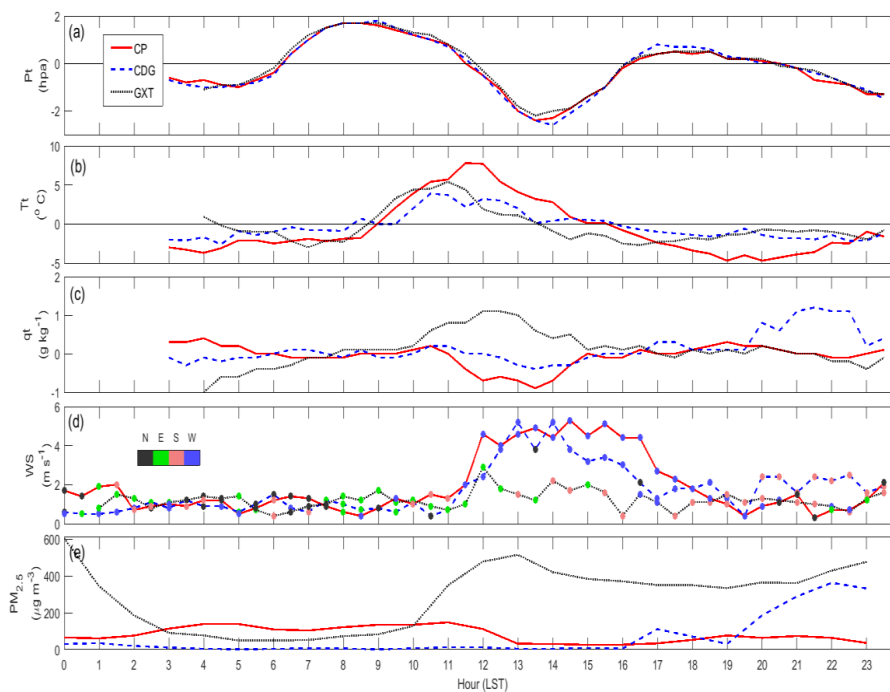
683

684 Figure 7. Same as Fig 6, but with relative humidity.

685

686

687



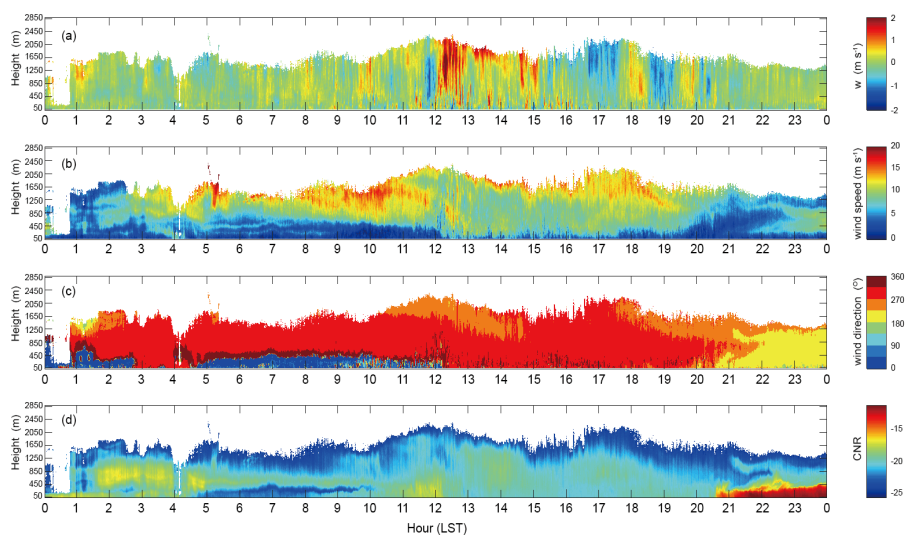
688

689 Figure 8. Three-hourly (a) pressure tendency, (b) air temperature tendency, and (c) specific
690 humidity, (d) wind speed (lines) and wind directions (colored dots), and (e) $PM_{2.5}$ concentration at
691 CP (red line), CDG (blue dash line) and GXT (black dash line) on 24 December 2015.

692



693

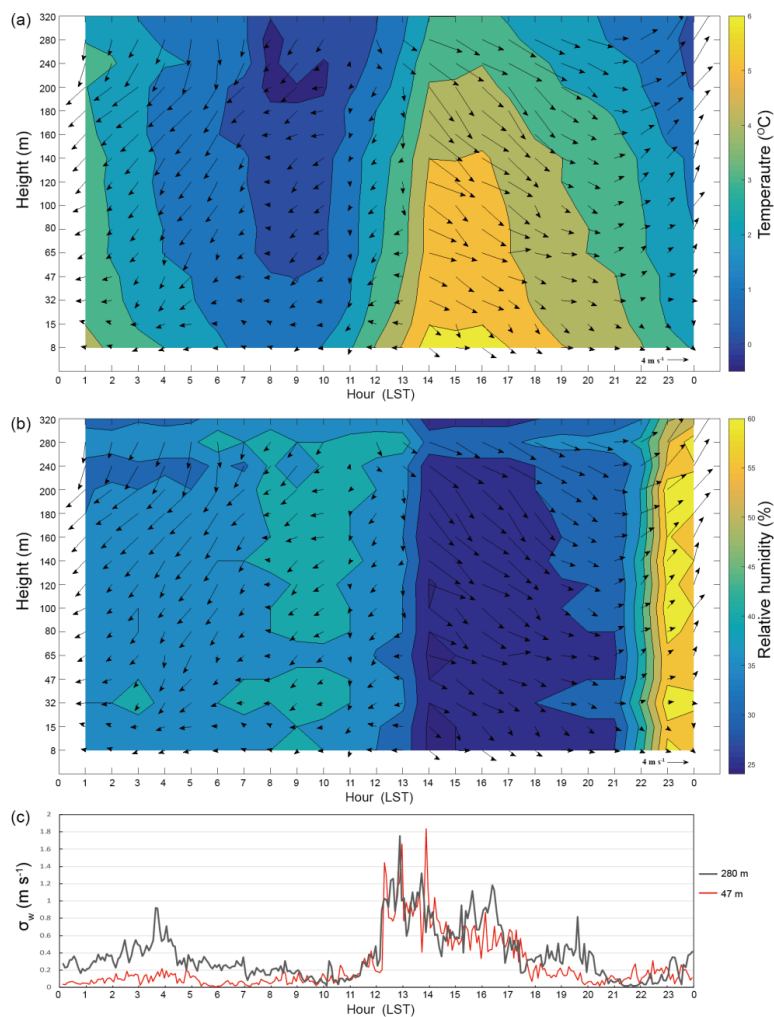


694

695 Figure 9. Doppler lidar observations of (a) vertical wind velocity, (b) horizontal wind speed, (c)
696 wind direction, and (d) carrier-noise-ratio (CNR) at IAP on 24 December 2015.

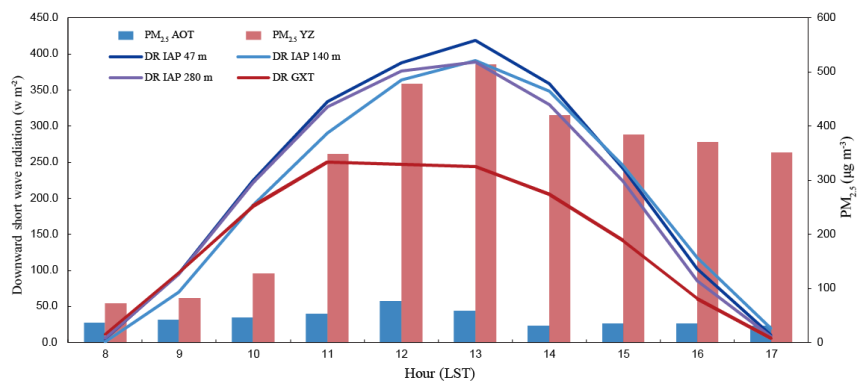
697

698



699
700 Figure 10. Temporal variations of (a) temperature (colored contours) and wind vectors, (b) relative
701 humidity (colored contours) and wind vectors at 15 levels on the IAP tower, and (c) vertical
702 velocity variance at 47 m and 280 m on the IAP tower on 24 December 2015.

703



704

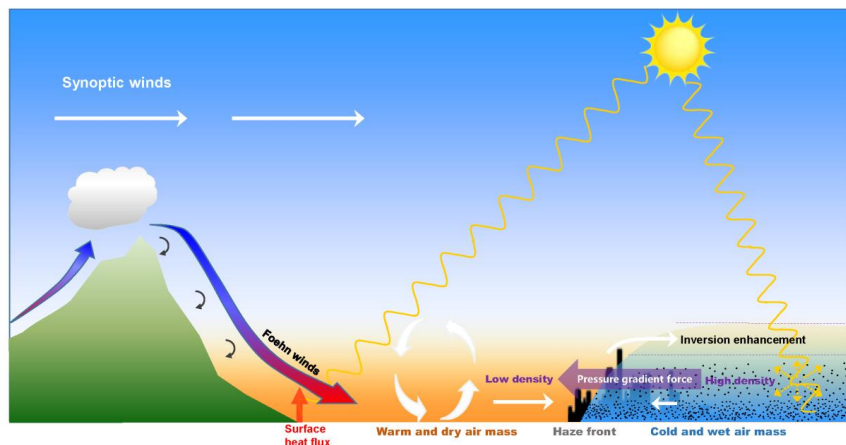
705 Figure 11. The temporal variations of PM_{2.5} concentrations at ATZX (blue bars),
706 and downward short-wave radiation at GXT and at heights of 47 m, 140 m and 280 m at the IAP
707 tower during daytime on 24 December 2015.

708

709



710



711

712 Figure 12. Schematic diagram of the haze front formation.

713

714